

**Rupture Characteristics and the Structural Control of the 2016 Mwp 6.1 Intraplate  
Earthquake in the Petermann Ranges, Australia**

Januka Attanayake<sup>1</sup>, Tamarah R. King<sup>1</sup>, Mark C. Quigley<sup>1</sup>, Gary Gibson<sup>1</sup>, Dan Clark<sup>2</sup>, Abraham  
Jones<sup>1</sup>, Sarah L. Brennand<sup>2, ¥</sup>, and Mike Sandiford<sup>1</sup>

Corresponding Author: Januka Attanayake ([januka.attanayake@unimelb.edu.au](mailto:januka.attanayake@unimelb.edu.au))

<sup>1</sup>School of Earth Sciences, University of Melbourne, Parkville, VIC 3010, Australia

<sup>2</sup> Geoscience Australia, Cnr Jerrabomberra Ave and Hindmarsh Drive, Symonston ACT 2609,  
Australia

<sup>¥</sup> now at the University of Queensland, Brisbane, QLD 4072, Australia

## Abstract

The 20<sup>th</sup> May 2016 Mwp 6.1 surface-rupturing intraplate earthquake in the Petermann Ranges is the largest earthquake to occur in the Australian continent in 19 years. We use *in situ* and InSAR surface observations, inversion of seismic second moments, and the distribution of aftershocks to determine source properties of the Petermann earthquake. Surface observations reveal a 21 km long surface rupture trace (strike =  $294^{\circ} \pm 29^{\circ}$ ) with heterogeneous vertical displacements ( $< 0.1$  m to 0.96 m). Inversion of apparent source time functions (ASTFs) computed from empirical Green's function deconvolution for seismic second moments yield rupture dimensions of the causative fault of average length ( $L_c$ ) = 17.40 km (95% confidence interval [14, 29] km) and width ( $W_c$ ) = 9.61 km [5, 15]. Using  $L_c$  and  $W_c$  estimates and fixing Mwp to 6.1, we infer a fault area of 167 km<sup>2</sup> (consistent with the spatial distribution of aftershocks) and an average slip  $\leq 0.45$  m. Our high frequency ASTFs are complex and potentially reflect the rupture of up to four asperities. The estimated stress drop of 0.42 MPa (95% confidence interval [0.10, 1.54] MPa) is low for an intraplate earthquake; we attribute this to low frictional slip (effective coefficient of friction  $> 0.002$ ) along rupture-parallel phyllosilicate-rich surfaces within the host rock fabric with possible additional contributions from elevated pore-fluid pressures. If the Petermann fault is characterised by long recurrence intervals, low friction may provide an explanation. Aftershock arrays suggest a triangular-shaped rupture plane (strike  $\approx 294$ , dip  $\approx 30^{\circ}$ ) that intersects the subsurface projection of the major geophysical structure (Woodroffe Thrust; WT) proximal to the preferred location of the mainshock hypocentre, suggesting the mainshock nucleated at a fault junction. Footwall seismicity includes apparent SW-dipping Riedel-type alignments including possible activation of the deep segment of the WT.

## Introduction

Continental intraplate earthquakes can cause disproportionately more damage than their interplate equivalents (Bilham, 2014) and the fault displacement hazard they pose may increase when accompanied by surface rupture (e.g. Yifan, 2008). Obtaining accurate measures of the dimensions, geometry, and slip of historical fault ruptures is important for comparative analysis with seismic moment estimates, refining source-moment scaling relationships (Leonard, 2010) and contributing to seismic hazard analyses (Allen et al., 2018). The Mwp 6.1 May 20<sup>th</sup> 2016 Petermann Ranges earthquake (henceforth Petermann earthquake) is the largest earthquake recorded in the Australian continent in 19 years. The remote location of the earthquake resulted in no damage or loss of life. In this study we integrate field and remotely-sensed observations of surface faulting and deformation, inversion of seismic second moments, and aftershock distributions to determine fault dimensions, geometry, and rupture characteristics (e.g. average slip and stress drop) of the Petermann Ranges earthquake. Our results reduce non-uniqueness in source parameters estimated in previous studies. We also present evidence for (i) sub-parallelism between bedrock fabrics and rupture orientation, and (ii) spatial associations between fault intersections, hypocenter location, and aftershock activity. Collectively these provide evidence for an influence of crustal geological structure on the rupture dynamics of the Petermann earthquake.

## Seismotectonics

Australia has experienced nine onshore events  $M_w > 6.0$  since 1910 (Fig. 1a, Allen et al., 2018) and averages two  $M_w > 5$  events per year (Leonard, 2008). Nine surface-rupturing earthquakes with  $4.7 \leq M_w \leq 6.6$  (including the one investigated here) have been reported since 1968 (Clark et al., 2014). Most  $M_w > 5.5$  historic events have occurred in remote cratonic Australia and caused no fatalities. However, hundreds of faults with potential neotectonic movement have been identified across the continent (Quigley et al., 2006; Clark et al., 2012), and the full historic earthquake catalogue highlights four zones of high-seismicity (Leonard, 2008; Allen et al., 2018), three of which are close to major cities (Perth, Adelaide, Melbourne).

The regional crustal stress field varies across the continent in response to distant Indo-Australian plate boundary forces (Coblentz et al., 1998; Rajabi et al., 2017). The Petermann earthquake occurred in the western Musgrave block (Fig. 1a), a Meso-Proterozoic basement province (Edgoose et al., 2004) near the Northern Territory, South Australia and Western Australia border with an approximate orientation of maximum horizontal present-day stress ( $SH_{max}$ ) of  $043^\circ$  (Rajabi et al., 2017). The earthquake ruptured through granitic mylonites on the hanging-wall of the SW dipping Woodroffe Thrust (WT), a major structure which controlled lower-crustal uplift and metamorphism during the 580-520 Ma Petermann Orogeny (Edgoose et al., 2004). The WT location and geometry is defined by regional geophysical maps (Edgoose et al., 2004, Raimondo, 2010) and seismic reflection profiles (Neumann, 2013). The mapped trace of the WT is approximately  $10 (\pm 3)$  km north of the surface rupture trace created by the Petermann

earthquake, dips approximately  $30^{\circ} (\pm 10^{\circ})$  SW (Neumann, 2013) and may be up to  $3 (\pm 1)$  km wide (Camacho et al., 1995; Raimondo, 2010, Edgoose et al., 2004).

The large gravity anomalies ( $\sim 150$  mgal) observed in this region were produced by Alice Springs (300 – 450 Ma) and Petermann (500 – 550 Ma) orogenies and they appear to reflect lithospheric strength (Beekman et al., 1997; Sandiford, 2002). The Petermann orogen is a large zone of deformation having dimensions of  $\sim 1500$  km (E-W) and  $\sim 300$  km (N-S) with an estimated N-S shortening exceeding 100 km, and possibly sustained a deformation rate of about 1.5 – 2 mm/yr over a 50 – 60 Ma period (Flöttmann et al., 2004, Raimondo et al., 2010). While the Woodroffe thrust appears to have accommodated a substantial part of this deformation, a precise estimate of the deformation rate is still lacking. Moreover, a clear relationship between the present-day gravitational anomalies and brittle deformation associated with this broad deformation zone is yet to be established (Copley, 2017).

## **Rupture Characteristics**

### **Surface Observations**

InSAR displacement fringes (Fig. 1a) for the Petermann earthquake highlight an approximately 21 km long surface rupture with a 7 km wide zone of hanging-wall deformation and  $< 3$  km wide zone of footwall deformation (Polcari et al., 2018). The zone of observed environmental damage is wider on the hanging-wall compared to the footwall (Fig. 1a). Along the 21 km rupture trace defined by InSAR, visible fault offset at the surface is discontinuous and highly variable in

intensity and morphology (Fig. 1b-e). The overall rupture has a slightly convex shape (relative to the epicenter) with strike deviating from  $\sim 280^\circ$  in the NW to  $\sim 303^\circ$  in the SE. We therefore describe the average fault strike as  $294^\circ \pm 29^\circ$ , derived from averages of the InSAR ( $288^\circ \pm 33^\circ$ ) and observable surface rupture traces ( $299^\circ \pm 25^\circ$ ).

High-accuracy elevation measurements along the visible surface rupture were obtained 5 weeks after the mainshock using a real time kinematic (RTK) GPS system (see Data and Resources section). From the RTK measurements, 104 vertical offset measurements were derived across the hanging-wall and foot-wall (Fig. 1a). From the RTK data, average vertical offset along the rupture is just 0.23 m (Fig. 1b), with a standard deviation  $\pm 0.18$  m and median of 0.18 m (Fig. 1c). Maximum vertical offset of 0.96 m occurs approximately 8 km (from the NW-most point) along the rupture (close to Fig. 1d). Within 180 m either side of this maximum value, vertical offset diminishes to  $< 0.1$  m. The second highest vertical offset of 0.72 m occurs 17 km along the rupture (close to Fig. 1e) and decreases to  $< 0.3$  m within 600 m either side. These vertical measurements may underestimate actual fault displacement, as they do not capture distributed deformation away from the surface rupture and lateral slip components.

#### Seismic Second-degree Polynomial Moments (S-DPMs) Inversion

If one assumes that earthquake moment release is confined to a 2-D fault plane, rupture length ( $L_c$ ) and width ( $W_c$ ) of a source can be determined from inverting S-DPMs (McGuire et al., 2001). Within this theoretical framework, the stress glut rate tensor ( $\Gamma(r, t)$ ) describes the spatial and temporal slip distribution of the earthquake and it can be modelled as  $\Gamma(r, t) = M f(r, t)$ ,

where  $M$  is the unit-norm moment tensor and  $f(r, t)$  is the scalar source space-time function. A double integration over the source volume and time relates S-DPMs to  $f(r, t)$ . For a comprehensive review of theory, the reader is referred to Backus and Mulcahy (1976). In this study, we used McGuire's (2017) implementation of the inversion to solve for  $L_c$  and  $W_c$ . We first compute apparent source time functions (ASTFs) for a set of azimuthally distributed stations using empirical Green's function (EGF) deconvolution (McGuire, 2004), and then invert these ASTFs for S-DPMs, from which rupture dimensions are estimated assuming a rectangular fault.

In the inversion, we used source locations provided in the Geoscience Australia catalog (see Data and Resources section) for the main event (25.579°S, 129.832°E, Mwp 6.1) and the EGF event (25.574°S, 129.812°E,  $M_L$  3.7). The latter is an aftershock that occurred within an hour of the main event. The lateral separation between the two events is about 2 km. Together with the difference in magnitudes, this short lateral distance between the two events provides ideal conditions for the EGF deconvolution procedure. We extracted a 1-D P wave velocity profile from the nearest node of the AusREM model (Kennett and Salmon, 2013) to the epicenter of the main event to compute temporal and spatial partial derivatives.

In total, we used data from 43 azimuthally distributed stations located within 1257 km epicentral distance (see Data and Resources section). Given the relatively small magnitude of the EGF event, seismograms with clear P waveforms were limited to this distance range. We removed the instrument response, converted waveforms to velocity, and applied a bandpass with corners 0.2 Hz and 5 Hz, capturing the spectral corner frequencies of both the events within this frequency band. The lower corner of our frequency band is determined by the spectral content of the EGF

event and the upper corner is the Nyquist frequency. Thus, our rupture models are based on information carried in a relatively higher frequency band. A uniform time window of 6.0 s trailing the onset of the P wave was selected for the deconvolution procedure, whereby we capture the main P wave energy and avoid contamination from higher order reverberations. Based on surface observations described earlier, we used the average strike of the fault plane ( $294^\circ \pm 29^\circ$ ) in our inversion.

In Fig. 2, we show example results of the EGF deconvolution along with ASTFs. We find that the ASTFs have a complex form and exhibit up to four main energy pulses (Fig. 3a), which we interpret as arising from the rupture of up to four asperities. This heterogeneous high frequency fault model is also consistent with irregular slip observed along the surface trace and lower confining pressure present at shallow hypocentral depth (1 - 5 km). For instance, our *in situ* observations indicate a zone of major deformation, a significant step over, and two segments of maximum uplift (Fig. 1). This is consistent with the InSAR image that exhibits multiple lineaments, suggesting a more complex scenario than the rupture of a single asperity. While our station coverage west of the epicenters is not ideal, ASTFs appear to be longer in the southeast direction, implying rupture propagation towards the northwest. The estimated second-moment dimensionless directivity parameter of 0.68 (0 - bilateral, 1 - unilateral, McGuire et al., 2002) imply some degree of unilaterality. Inverting these ASTFs produced  $L_c = 17.40$  km and  $W_c = 9.61$  km. We also conducted bootstrap computations to determine the 95% confidence interval of  $L_c$  and  $W_c$  with 5000 iterations. They are;  $L_c = [14, 29]$  and  $W_c = [5, 15]$ . These results are shown in Fig. 3b.



Given that the nearest stations in Alice Springs are located  $\sim 450$  km from the main and the EGF events, the earthquake depths are poorly constrained. 3-D waveform inversions suggest that the best-fitting centroid location is 1 km deep (Hejrani and Tkalčić, 2019). As we show in our next section, hypocentral depths of these earthquakes are unlikely to be greater than 5 km. To test the sensitivity of  $L_c$  and  $W_c$  to event depths, we conducted inversions by systematically varying event depths in the range 0 – 5 km and find that  $L_c$  and  $W_c$  are not affected. Another uncertainty in  $L_c$  and  $W_c$  arises from the variation in strike. As we report here, the variability of strike is  $\pm 29^\circ$ , which results in a variation of  $\pm \sim 2$  km and  $\pm \sim 1$  km in  $L_c$  and  $W_c$  respectively.

#### Aftershock Distribution

Beginning three days after the Petermann earthquake, Geoscience Australia (GA) and the University of Melbourne started installing a temporary seismic network of nine stations in the vicinity of the main earthquake. From the data recorded by these stations, we precisely located 69 events with  $-0.2 \leq M_L \leq 3.5$  using the eqFocus software (Attanayake et al., 2019). In this method, we hand-picked P and S phase arrivals, computed travel time predictions using a local velocity model (TC1A, see Data and Resources section), and handled the inversion using the Levenberg-Marquardt minimization procedure. Owing to the distance to the nearest station being smaller than the hypocentral depth, the average depth uncertainty is only  $\pm 0.37$  km in this dataset (see Data and Resources section). The distribution of these aftershocks is shown in Fig. 4a. It is evident that aftershocks located east of the surface trace define a fault plane with an average dip of  $\sim 30^\circ$  to the northeast (Fig. 4b). Activity on this fault plane appears to be contained within the uppermost 7 km of the crust. The depth to the fault below the epicentre of the main

earthquake is  $\sim 3$  km, consistent with the shallow centroid depth estimated in previous studies (e.g. Hejrani and Tkalčić, 2019). The aftershocks located west of the surface trace appear to align with the projected plane of the WT that dips to the southwest. The Petermann earthquake epicentre overlies the intersection of the projected WT and the Petermann aftershock lineament; this spatial overlap suggests the possibility that the Petermann earthquake nucleated proximal to or within this fault junction zone, as observed for many crustal earthquakes (Talwani, 1999; Gabrielov et al., 1996; Quigley et al., 2019). Another intriguing observation is the sets of SW-dipping aftershock arrays parallel to the WT, but deeper within the footwall of the Petermann earthquake source fault (Fig. 4b); the  $\sim 30^\circ$  counter-clockwise orientation with respect to the Petermann fault is consistent with the expected orientations of early en échelon Riedel shears (Tchalenko, 1970).

## Discussion

The aftershock distribution provides key information regarding the geometry of the causative fault, defining a plane dipping to the northeast with an angle of  $\sim 30^\circ$ . This differs from the optimal dip angles reported in InSAR inversions of  $39^\circ$  (Polcari et al., 2018) and  $22^\circ$  (Wang et al., 2019) and the GCMT catalog estimate of  $45^\circ$ . While these source inversions have produced variable dip angles possibly due to different data sensitivities, *in situ* measurements of rock foliations indicate an average dip angle  $\sim 30^\circ$  (Scrimgeour et al., 1990, dip angles in Fig. 4), lending confidence to our estimate. The environmental seismic intensity (ESI) level IX contour in Fig. (4) roughly encloses the active fault area defined by the aftershock distribution east of the surface trace. This area is estimated to be  $\sim 158 \text{ km}^2$  ( $1/2 \times$  length of surface trace (21 km)  $\times$

down-dip extent of aftershocks ( $\sim 15$  km)). In comparison, seismic second moments-derived constraints on  $L_c$  and  $W_c$  yield an estimate of  $\sim 166$  km<sup>2</sup> for a rectangle fault area ( $L_c \times W_c$ ) that independently validate this approximate source size.

Using GA's moment magnitude (Mwp 6.1) of the Petermann earthquake (see Data and Resources section), we estimate an average slip  $\leq 0.45$  m for this rupture using the standard equation  $M_0 = \mu A d$ , where  $M_0$  is the seismic moment,  $\mu$  is dynamic shear modulus estimated from density  $\times$  (shear velocity)<sup>2</sup> at the source,  $A$  is fault area, and  $d$  is average slip. In this calculation, we used 2608 kg/m<sup>3</sup> and 3.3 km/s, respectively, for density and shear velocity from the AusREM model (Kennett and Salmon, 2013). In comparison to our estimates, the source models inverted from InSAR measurements (Polcari et al., 2018; Wang et al., 2019) yield larger estimates of average slip ( $\sim 1$  m) and smaller fault areas ( $\sim 45 - 75$  km<sup>2</sup>). This is probably because these models attempt to fit the observed maximum surface deformation of  $\sim 1$  m in a half-space model with uniform slip rather than distributed slip on a heterogeneous fault plane. Our *in situ* observations clearly demonstrate surface expressions of fault heterogeneity in terms of fault strike and vertical displacement.

Our estimate of fault area allows us to determine stress drop and its uncertainty of the Petermann earthquake. By assuming **Mwp = 6.1**, we estimate the stress drop ( $\Delta\sigma$ ) of the main earthquake to be **0.42 MPa**. The uncertainty range of  $\Delta\sigma$  (**0.10 – 1.54 MPa**) is estimated by considering the 95% confidence interval of rupture dimensions, where  **$0.17 \text{ m} \leq d \leq \sim 1 \text{ m}$**  (observed peak displacement). In these calculations, we set  $\Delta\sigma = (7/16) \times (M_0/r^3)$ , where  $r = (L_c \times W_c)^{1/2}$  (Kanamori and Anderson, 1975). The  $\Delta\sigma = \mathbf{0.42 \text{ MPa}}$  is significantly lower than the stress drops

estimated for several well-recorded recent earthquakes in the Australian continent (20-50 MPa) (Dawson et al., 2008; Attanayake et al., 2019) and the global median for intraplate earthquakes of  $\sim 6 (\pm 1)$  MPa (Allmann and Shearer, 2009).

The low  $\Delta\sigma$  could be explained by a weak crust with low differential stress (Hardebeck and Aron, 2009) and/or a low-friction rupture at shallow depths (Copley and Woodcock, 2016). Western and central Australia are generally characterised by low Lg wave attenuation (Wei et al., 2017), high predicted stress magnitudes (25 to 50 MPa; Coblenz et al., 1998), and earthquakes with high stress drops (e.g., 27 – 53 MPa in Mw 4.7 Katanning earthquake in Western Australia; Dawson et al., 2008). Collectively these observations suggest high crustal strength, **eliminating weak crust as an explanation**. On the other hand, previous mapping (Scrimgeour et al., 1999; Camacho et al., 1995; Wex et al., 2019) and our field observations of rupture-parallel, biotite mica-rich mylonitic layers in bedrock outcrops adjacent to the surface rupture (Fig. 1d) provide a plausible mechanism for low-friction faulting in the Petermann earthquake. Intrinsic heterogeneities such as the presence of phyllosilicate-rich foliations and/or elevated pore pressures can reduce the frictional strength of faults, producing lower  $\Delta\sigma$  (Collettini et al., 2009; Copley, 2017). The mechanical behaviour of phyllosilicate layers provides a fault weakening mechanism for generating lower  $\Delta\sigma$  ruptures (Shea Jr. and Kronenberg, 1993). In addition, elevated pore pressures, possibly related to water-enhanced inter-layers between less permeable phyllosilicate barriers, might also have played a role in fault weakening prior to or during rupture. Testing this hypothesis requires further analysis of possible subsurface hydrologic conditions in the source region beyond that presented by Wang et al., (2019).

By assuming that estimated  $\Delta\sigma$  represents a complete stress release, we compute the coefficient of friction ( $\mu$ ) of the Petermann fault - a proxy for fault strength. If, however, the Petermann earthquake released accumulated stress partially, this estimate is a lower bound to  $\mu$ . We used the formulation of Suppe (2014) for computing  $\mu$ :  $\sigma_1 - \sigma_3 = \kappa(\rho_r - \rho_w)gh$  and  $\kappa = 2[\sin(\varphi) - \sin^2(\varphi)]$ , where  $\varphi = \text{atan}(\mu)$ . Here,  $\sigma_1 - \sigma_3$  is the maximum differential stress ( $= \Delta\sigma$ ),  $\rho_r$  and  $\rho_w$  are, respectively, the bulk density of the crust ( $2800 \text{ kgm}^{-3}$ ) and water ( $1000 \text{ kgm}^{-3}$ ),  $g$  is gravitational acceleration ( $9.81 \text{ ms}^{-2}$ ), and  $h$  is hypocentral depth ( $1 - 5 \text{ km}$ ). Note that  $\mu$  is an effective value as we incorporate hydrostatic pore-fluid pressure in this computation and our estimate is  $0.002$  ( $h=5 \text{ km}$ )  $\leq \mu \leq 0.12$  ( $h=1 \text{ km}$ ). This lower bound to  $\mu$  is significantly less than widely used laboratory estimates ( $0.6 - 0.85$ ) of Byerlee (1978) yet it is consistent with upper bounds to  $\mu$  ( $0.02 - 0.24$ ) estimated for intraplate reactivated thrust faults from regional scale force balance computations (Copley and Woodcock, 2016). Our low estimates of  $\mu$  are also in accord with more recent rotary shear experimental predictions ( $\mu \rightarrow 0$ ) at realistic slip rates (Di Toro et al., 2004). If the Petermann fault is weak as we infer here, it might be characterised by long recurrence intervals because accumulation of stress on the fault is impeded by low friction.

The alignment of deep footwall aftershocks with the projected WT (Fig. 4b), suggest localized seismic activation of this structure. Static and dynamic stress transfer (Freed, 2005) from the Petermann earthquake and/or other changes in fault structure or pore pressures might have been responsible for this observation. The triangular-shaped rupture plane intersects WT proximal to the preferred location of the Petermann earthquake hypocentre, suggesting the earthquake may have nucleated at this fault junction. Finally, the presence of apparent Riedel shears identified by short arrays of aftershocks in the footwall contributes to our understanding of the complex

structural fabrics that may be created/**reactivated** and enhanced by crustal earthquakes. Further monitoring of seismicity in the source region can provide a better picture of these apparent pervasive footwall structures.

## **Data and Resources**

Source parameters of the main earthquake was obtained from the Geoscience Australia catalog <https://earthquakes.ga.gov.au/> (last accessed 25.04.2019). The GCMT catalog can be found at <https://www.globalcmt.org/CMTsearch.html> (last accessed 29.04.2019). Seismic waveforms for the main and EGF earthquakes were downloaded from the Incorporated Research Institutes for Seismology (IRIS) Wilber 3 website [https://ds.iris.edu/wilber3/find\\_event](https://ds.iris.edu/wilber3/find_event) (last accessed 18.12.2018). The in situ RTK vertical displacement measurements, **TC1A crustal velocity model**, and the aftershock catalog are available at <https://github.com/unimelb-geophysics/Petermann-Ranges> (Last accessed 15.08.2019). All figures except Fig. 1 were made with Generic Mapping Tools, Version 5.4.2 (Wessel et al., 2013). The seismograms were pre-processed with Seismic Analysis Code (Goldstein et al., 2003)

## **Acknowledgments**

The University of Melbourne's (UoM) temporary seismic array was funded by AuScope's Australian Geophysical Observing System (AGOS) Subsurface Observatory through an Education Investment Fund (EIF) grant. Geoscience Australia contributed data from four additional seismographs to the study. Also, Geological Survey of South Australia (GSSA) contributed some equipment to the UoM temporary array. MQ is supported by the Australian Research Council through Discovery Grant number DP170103350, and TRK through the

Australian Government Research Training Program Scholarship. DC and SLB publish with the permission of the CEO of Geoscience Australia. Comments made by the associate editor Cezar Tifu and two anonymous reviewers improved this manuscript significantly.

## References

Allen, T., J. Griffin, M. Leonard, D. Clark, and Ghasemi, H., 2018. The 2018 National Seismic Hazard Assessment for Australia: model overview, Geoscience Australia Record 2018/27, Canberra, 126 pp, doi: 10.11636/Record.2018.027.

Allmann, B. P., and P. M. Shearer (2009). Global variations of stress drop for moderate to large earthquakes, J. Geophys. Res., **114** B01310. doi:10.1029/2008JB005821.

Attanayake, J. D. Sandiford, L. S. Schleicher, A. Jones, G. Gibson, and M. Sandiford (2019). Interacting intraplate fault systems in Australia: The Thorpdale, Victoria seismic sequences, J. Geophys. Res., <https://doi.org/10.1029/2018JB016945>

Backus, G. and M. Mulcahy (1976). Moment tensors and other phenomenological descriptions of seismic sources—I. Continuous displacements, Geophys. J. R. astr. Soc., 46, 341–361.

Beekman, F., R. A. Stephenson, and R. J., Korsch, (1997). Mechanical stability of the Redbank Thrust Zone, Central Australia: Dynamic and rheological implications, Australian Journal of Earth Sciences, 44(2), 215 – 226.

345 Bilham, R., (2014). Aggravated earthquake risk in South Asia: Engineering versus human nature.  
 346 In M. Wyss (Ed.), *Earthquake hazard, risk, 60 and disasters*, (pp. 103–141). Amsterdam:  
 347 Elsevier. <https://doi.org/10.1016/B978-0-12-394848-9.00005-5>  
 348  
 349 **Byerlee, J., 1978. Friction of rocks. *Pure Appl. Geophys.* 116, 615–626.**  
 350  
 351 Camacho, A., Vernon, R. H., and J. D. Fitzgerald (1995). Large volumes of anhydrous  
 352 pseudotachylite in the Woodroffe Thrust, eastern Musgrave Ranges, Australia, *Journal of*  
 353 *Structural Geology*, **17** 371 – 383.  
 354  
 355 Clark, D., A. McPherson, and R. Van Dissen (2012). Long-term behaviour of Australian stable  
 356 continental region (SCR) faults, *Tectonophysics*, **566 – 567** 1 – 30.  
 357 <http://dx.doi.org/10.1016/j.tecto.2012.07.004>  
 358  
 359 Clark, D., A. Mcpherson, and T. Allen (2014). Intraplate earthquakes in Australia. In P. Talwani  
 360 (Ed.), *Intraplate earthquakes*, (pp. 8–49). Cambridge: Cambridge University Press.  
 361 <https://doi.org/10.1017/CBO9781139628921.012>  
 362  
 363 Coblenz, D. D., Zhou, S., Hillis, R., Richardson, R., and Sandiford, M. (1998). Topography,  
 364 plate-boundary forces and the Indo-Australian intraplate stress field. *J. Geophys. Res.*, **103(B1)**  
 365 919 –931. <https://doi.org/10.1029/97JB02381>  
 366



367 Collettini, C., A. Niemeijer, C. Viti, and C. Marone (2009). Fault zone fabric and fault weakness,  
 368 Nature, **462** 907 – 910.  
 369

370 Copley, A., and N. Woodcock (2016). Estimates of fault strength from the Variscan foreland of  
 371 the northern UK, Earth Planet. Sci. Lett., **451** 108 – 113.  
 372 <http://dx.doi.org/10.1016/j.epsl.2016.07.024>  
 373

374 Copley, A. (2017). The strength of earthquake-generating faults, Journal of the Geological  
 375 Society, **175(1)** 1. <http://dx.doi.org/10.1144/jgs2017-037>  
 376

377 Dawson, J., P. Cummins, P. Tregoning, and M. Leonard (2008). Shallow intraplate earthquakes  
 378 in Western Australia observed by Interferometric Synthetic Aperture Radar, J. Geophys. Res.,  
 379 **113** B11408, doi:10.1029/2008JB005807  
 380

381 Di Toro, G., D. L. Goldsby and Terry E. Tullis (2004). Friction falls towards zero in quartz rock  
 382 as slip velocity approaches seismic rates, Nature, **427**, 436 – 439.  
 383

384 Edgoose, C.J., I. R. Scrimgeour, and D. F. Close (2004). Geology of the Musgrave Block,  
 385 Northern Territory. Northern Territory Geological Survey.  
 386

387 Freed, A. M. (2005). Earthquake triggering by static, dynamic, and postseismic stress  
 388 transfer, Annu. Rev. Earth Planet. Sci., **33** 335 – 367.  
 389

- Flöttmann, T., M. Hand, D. Close, C. Edgoose, and I. R. Scrimgeour (2004). Thrust tectonic styles of the intracratonic Alice Springs and Petermann orogenies, central Australia, *in* *Thrust Tectonics and Hydrocarbon Systems*, edited by K. McClay, AAPG Mem., 82, 538–557.
- Gabrielov, A., V. Keilis-Borok, and D. D. Jackson (1996). Geometric incompatibility in a fault system. *Proceedings of the National Academy of Sciences*, **93**(9) 3838-3842.
- Goldstein, P., Dodge, D., Firpo, M., & Minner, L. (2003). SAC2000: Signal processing and analysis tools for seismologists and engineers. In W. H. K. Lee, H. Kanamori, P. C. Jennings, & C. Kisslinger (Eds.), *Invited contribution to the IASPEI international handbook of earthquake and engineering seismology*, (pp. 1613–1614). London: Academic Press.
- Hardebeck, J., and A. Aron (2009). Earthquake stress drops and inferred fault strength on the Hayward Fault, east San Francisco Bay, California, *Bull. Seism. Soc. Am.*, **99**(3) 1801 – 1814. doi: 10.1785/0120080242
- Hejrani, B., and H. Tkalčić (2019). The 20 May 2016 Petermann Ranges earthquake: centroid location, magnitude, and focal mechanism from full waveform inversion, *Australian Journal of Earth Sciences*, **66**(1) 37 – 45. <https://doi.org/10.1080/08120099.2018.1525783>
- Kanamori, H., and D. L. Anderson (1975). Theoretical basis of some empirical relations in Seismology, *Bull. Seism. Soc. Am.*, **65**(5) 1073 – 1095.

413 Kennett, B., and M. Salmon (2013). AuSREM: Australian Seismological Reference Model,  
 414 Australian Journal of Earth Sciences, **59** 1091-1103. doi: 10.1080/08120099.2012.736406  
 415  
 416 King, T. R., M. Quigley, and D. Clark (2018). Earthquake environmental effects produced by the  
 417 Mw 6.1, 20<sup>th</sup> May 2016 Petermann earthquake, Australia, Tectonophysics, **747 – 748** 357 – 372.  
 418 <https://doi.org/10.1016/j.tecto.2018.10.010>  
 419  
 420 Leonard, M. (2008). One hundred years of earthquake recording in Australia. Bull. Seism. Soc.  
 421 Am. **98** 1458–1470. <https://doi.org/10.1785/0120050193>  
 422  
 423 Leonard, M. (2010). Earthquake fault scaling: Self-consistent relating of rupture length, width,  
 424 average displacement, and moment release, Bull. Seism. Soc. Am., **100(5A)** 1971 - 1988. doi:  
 425 10.1785/0120090189  
 426  
 427 McGuire, J. J., L. Zhao, and T. H. Jordan (2001). Teleseismic inversion for the second-degree  
 428 moments of earthquake space-time distributions, Geophys. J. Int., **145** 661 – 678.  
 429  
 430 McGuire, J. J., L. Zhao, and T. H. Jordan (2002). Predominance of unilateral rupture for a  
 431 catalog of large events, Bull. Seism. Soc. Am., **92(8)** 3309 – 3317.  
 432  
 433 McGuire, J. (2004). Estimating finite source properties of small earthquake ruptures, Bull.  
 434 Seism. Soc. Am., **94(2)** 377 – 393.  
 435

436 McGuire, J. (2017). A MATLAB Toolbox for estimating the second moments of earthquake  
 437 ruptures, *Seism. Res. Lett.*, **88(2A)** 371 – 378. <https://doi.org/10.1785/0220160170>  
 438  
 439 Neumann, N.L. (Ed.) (2013). Yilgarn Craton – Officer Basin – Musgrave Province (YOM)  
 440 Seismic and MT Workshop, Record 2013/28. Geoscience Australia, Canberra, ACT.  
 441  
 442 Polcari, M., M. Albano, S. Atzori, C. Bignami, and S. Stramondo (2018). The causative fault of  
 443 the 2016 Mwp 6.1 Petermann Ranges intraplate earthquake (Central Australia) retrieved by C-  
 444 and L-band InSAR data, *Remote Sens.*, **10** 1311. doi:10.3390/rs10081311  
 445  
 446 Quigley, M. C., M. L. Cupper, and M. Sandiford (2006). Quaternary faults of south-central  
 447 Australia: palaeoseismicity, slip rates and origin, *Australian Journal of Earth Sciences*, **53** 285 –  
 448 301, <https://doi.org/10.1080/08120090500499271>  
 449  
 450 Quigley, M. C., A. Jiménez, B. Duffy, and T. R. King (2019). Physical and statistical behaviour  
 451 of multifault earthquakes, Darfield earthquake case study, New Zealand, *J. Geophys. Res.*, **124**.  
 452 <https://doi.org/10.1029/2019JB017508>  
 453  
 454 Raimondo, T., A.S. Collins, M. Hand, A. Walker-Hallam, R.H. Smithies, P.M. Evins, and H.M.  
 455 Howard (2010). The anatomy of a deep intracontinental orogen. *Tectonics* **29(4)**.  
 456 <https://doi.org/10.1029/2009TC002504>  
 457

458 Rajabi, M., M. Tingay, O. Heidbach, R. Hillis, and S. Renolds (2017). The present-day stress  
 459 field of Australia, *Earth-Science Reviews.*, **168** 165-189,  
 460 <http://dx.doi.org/10.1016/j.earscirev.2017.04.003>.  
 461  
 462 Sandiford, M. (2002). Low thermal Peclet number intraplate orogeny in central Australia, *Earth*  
 463 *Planet. Sci. Lett.*, **201** 309 – 320.  
 464  
 465 Scrimgeour, I.R., D. F. Close, and C. J. Edgoose (1999). Petermann Ranges SG52-7; explanatory  
 466 notes. Darwin.  
 467  
 468 Shea Jr., W. T., and A. K. Kronenberg (1993). Strength and anisotropy of foliated rocks with  
 469 varied mica contents, *Journal of Structural Geology*, **15(9 – 10)** 1097 – 1121. [https://doi-](https://doi-org.ezp.lib.unimelb.edu.au/10.1016/0191-8141(93)90158-7)  
 470 [org.ezp.lib.unimelb.edu.au/10.1016/0191-8141\(93\)90158-7](https://doi-org.ezp.lib.unimelb.edu.au/10.1016/0191-8141(93)90158-7)  
 471  
 472 Stewart, A. J. (1995). Western extension of the Woodroffe Thrust, Musgrave Block, central  
 473 Australia, *Journal of Australian Geology and Geophysics*, **16(1 – 2)** 147 – 153.  
 474  
 475 Suppe, J., (2014). Fluid overpressures and strength of the sedimentary upper crust, *Journal of*  
 476 *Structural Geology*, **69(B)**, 481 – 492. <https://doi.org/10.1016/j.jsg.2014.07.009>  
 477  
 478 Talwani, P. (1999). Fault geometry and earthquakes in continental interiors, *Tectonophysics*, **305**  
 479 371 – 379.  
 480

481 Tchalenko, J. S. (1970). Similarities between shear zones of different magnitudes, Geological  
482 Society of America Bulletin, **81** 1625 – 1640.

483

484 Wang, S., W. Xu, C. Xu, Z. Yin, R. Bürgmann, L. Liu and G. Jiang (2019). Changes in  
485 groundwater level possibly encourage shallow earthquakes in central Australia: The 2016  
486 Petermann Ranges earthquakes, Geophys. Res. Lett., **46(6)** 3189 – 3198.  
487 <https://doi.org/10.1029/2018GL080510>

488

489 Wei, Z., B. L. N. Kennett, and L. F. Zhao (2017). Lg-wave attenuation in the Australian  
490 crust, Tectonophysics, **717** 413-424.

491

492 Wex, S., N. S. Mancktelow, A. Camacho, and G. Pennacchioni (2019). Interplay between  
493 seismic fracture and aseismic creep in the Woodroffe Thrust, central Australia – Inferences for  
494 the rheology of relatively dry continental mid-crustal levels, Tectonophysics, **758** 55 – 72.  
495 <https://doi.org/10.1016/j.tecto.2018.10.024>

496

497 Wessel, P., W. H. F. Smith, R. Scharroo, J. Luis, and F. Wobbe (2013). Generic Mapping Tools:  
498 Improved Version Released, EOS Trans. AGU, **94(45)** 409-410. doi:10.1002/2013EO450001.

499

500 Yifan, Y. (2008). Impact of intensity and loss assessment following the great Wenchuan  
501 earthquake, Earthq. Eng. and Eng. Vib., **7** 247 - 254.

502

503

504    **Full Mailing Addresses**

505    JA., TRK., GG, MQ, AJ, MS

506    School of Earth Sciences

507    University of Melbourne

508    Parkville

509    VIC 3010

510    Australia

511

512    DC and SLB<sup>‡</sup>

513    Geoscience Australia

514    Cnr Jerrabomberra Ave and Hindmarsh Drive

515    Symonston

516    ACT 2609

517    Australia

518

519    <sup>‡</sup> Now at

520    University of Queensland

521    Brisbane

522    QLD 4072

523    Australia

524

525

526

## List of Figure Captions

**Figure 1.** Surface observations of the 2016 Petermann Thrust (PT) surface rupture. (a) map showing: the surface trace of both InSAR defined rupture, and where rupture is observable at the surface; RTK derived vertical offset measurements are shown as red circles scaled to the magnitude of offset; the epicentres of the main and EGF events as green and grey stars respectively; locations of photos. Inset maps show: the locations of  $M_w > 6.0$  since 1910 and the outline of the Musgrave Block; InSAR for the Petermann earthquake; and ESI-07 contours as described in King et al. (2018). Also shown are *in situ* RTK measurements along the strike. (b) – (e) photos demonstrating variation in offset and morphology of the surface rupture, with white arrows pointing along the bottom of the rupture, labels indicating the hanging-wall and foot-wall, and vertical offset from RTK measurements closest to the photo locations. Photos (b) and (c) were taken 20 days after the mainshock near the middle of the surface rupture. Photos (d) and (e) were taken 16 months after the mainshock, in the vicinity of the largest vertical offset measurements. The exposed basement rock outcrop circled in (d) has foliations oriented parallel to the arrows showing the surface rupture.

**Figure 2.** Example EGF deconvolution results for four stations: AS03 (top left), BBOO (top right), WB2 (bottom left), and MEEK (bottom right). For each station, the left panel shows seismograms for the main event (brown trace) and the EGF (yellow trace) with magnification. Also, station azimuth ( $\phi$ ) and epicentral distance ( $\Delta^\circ$ ) are also included. The right panel of each station shows the Apparent Source Time Function (ASTF) and the fit of  $ASTF \cdot EGF$  (red) to



data (black), where \* denotes the convolution operator. All waveforms are normalized by respective peak amplitudes.

**Figure 3.** Results of deconvolution and bootstrapping. (a) A representative azimuthal distribution of ASTFs (blue traces) plotted at the locations of stations (blue triangles). The epicentre (red star) of the main earthquake is also shown. Note that for clarity, not all ASTFs and stations used in the study are plotted. The average strike ( $294^{\circ}$ ) of the fault is projected across the continent (black dashed-line) to illustrate station distribution relative to the fault plane. ASTFs have a complex form and appear to be longer in the southeast direction (b) shows inversion results of  $L_c$  and  $W_c$  along with bootstrap calculations with 5000 iterations. The brown curve represents the equivalent normal distribution and the black dashed-lines show the 95% confidence interval.

**Figure 4.** The distribution of aftershocks. (a) Map showing the aftershock distribution (solid circles) color-coded by depth along with the surface trace of the Petermann Ranges earthquake (PT) and the Woodroffe Thrust (WT). The epicentres of the main and EGF events are shown with green and grey stars respectively. Six temporary seismic stations are also shown (blue triangles) while the other three stations are out of the field of view. The depth of aftershocks located to the east of PT increases to the northeast. The environmental seismic intensity (ESI) level IX is represented by the green contour (King et al., 2018). The strike and dip of foliation is from Scrimgeour et al. (1999). The area outlined in Fig. 1 of deformation detected by InSAR

image is outlined by dashed-lines. (b) The aftershocks projected on to a cross section along the AB profile shown in (a), which is approximately orthogonal to the average strike of PT. The purple solid line is fitted to color-coded aftershocks using a least squares method, from which the fault dip ( $30^\circ$ ) is estimated (The dotted line is horizontal). The reduced  $\chi^2$  for the least squares fit is also given. The inverted triangles show the surface intersections of PT (orange) and WT (dark grey). The orange dashed-line is arbitrarily drawn to connect PT with the underlying fault plane. The white circles with blue outlines are aftershocks located west of PT. They align with the projected fault plane of WT (dark grey dash-dot line) with a dip of  $20^\circ$  but the dip could vary between  $20^\circ - 30^\circ$  (Stewart, 1995; Neumann, 2013). The grey small arrows point to possible Riedel shears in the foot wall delineated by aftershocks.

# Figures

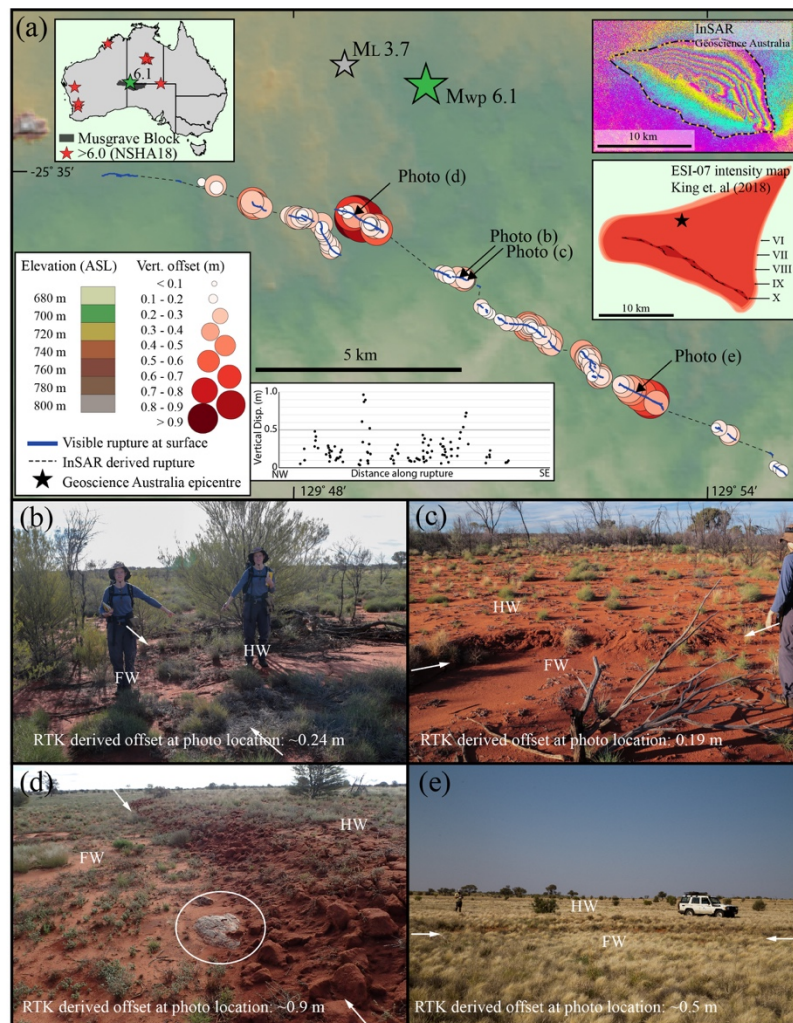


**Figure 1.** Surface observations of the 2016 Petermann Thrust (PT) surface rupture. (a) map showing: the surface trace of both InSAR defined rupture, and where rupture is observable at the surface; RTK derived vertical offset measurements are shown as red circles scaled to the magnitude of offset; the epicentres of the main and EGF events as green and grey stars respectively; locations of photos. Inset maps show: the locations of Mw > 6.0 since 1910 and the outline of the Musgrave Block; InSAR for the Petermann earthquake; and ESI-07 contours as described in King et al. (2018). Also shown are *in situ* RTK measurements along the strike. (b) –

(e) photos demonstrating variation in offset and morphology of the surface rupture, with white arrows pointing along the bottom of the rupture, labels indicating the hanging-wall and foot-wall, and vertical offset from RTK measurements closest to the photo locations. Photos (b) and (c) were taken 20 days after the mainshock near the middle of the surface rupture. Photos (d) and (e) were taken 16 months after the mainshock, in the vicinity of the largest vertical offset measurements. The exposed basement rock outcrop circled in (d) has foliations oriented parallel to the arrows showing the surface rupture.

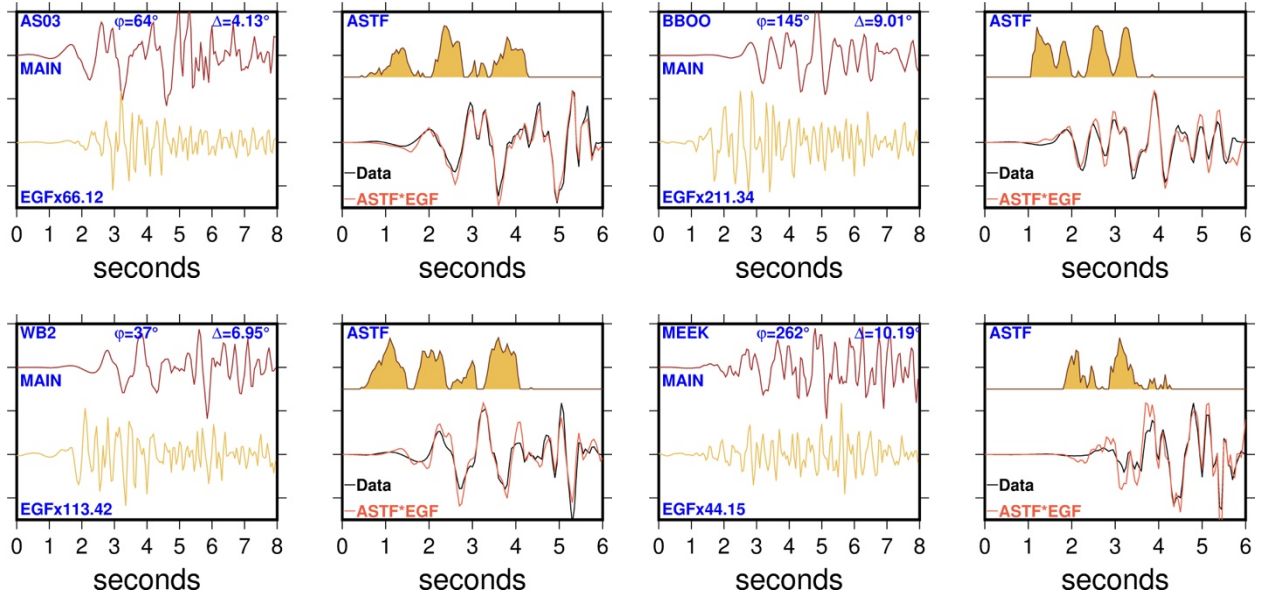
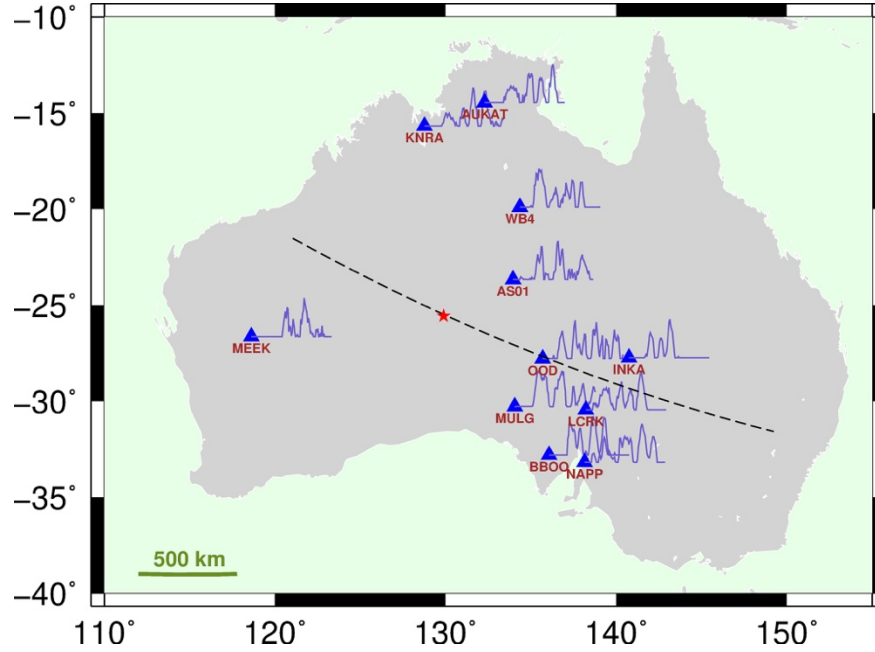


**Figure 2.** Example EGF deconvolution results for four stations: AS03 (top left), BBOO (top right), WB2 (bottom left), and MEEK (bottom right). For each station, the left panel shows seismograms for the main event (brown trace) and the EGF (yellow trace) with magnification. Also, station azimuth ( $\phi$ ) and epicentral distance ( $\Delta^\circ$ ) are also included. The right panel of each station shows the Apparent Source Time Function (ASTF) and the fit of ASTF\*EGF (red) to data (black), where \* denotes the convolution operator. All waveforms are normalized by respective peak amplitudes.

(a)



(b)

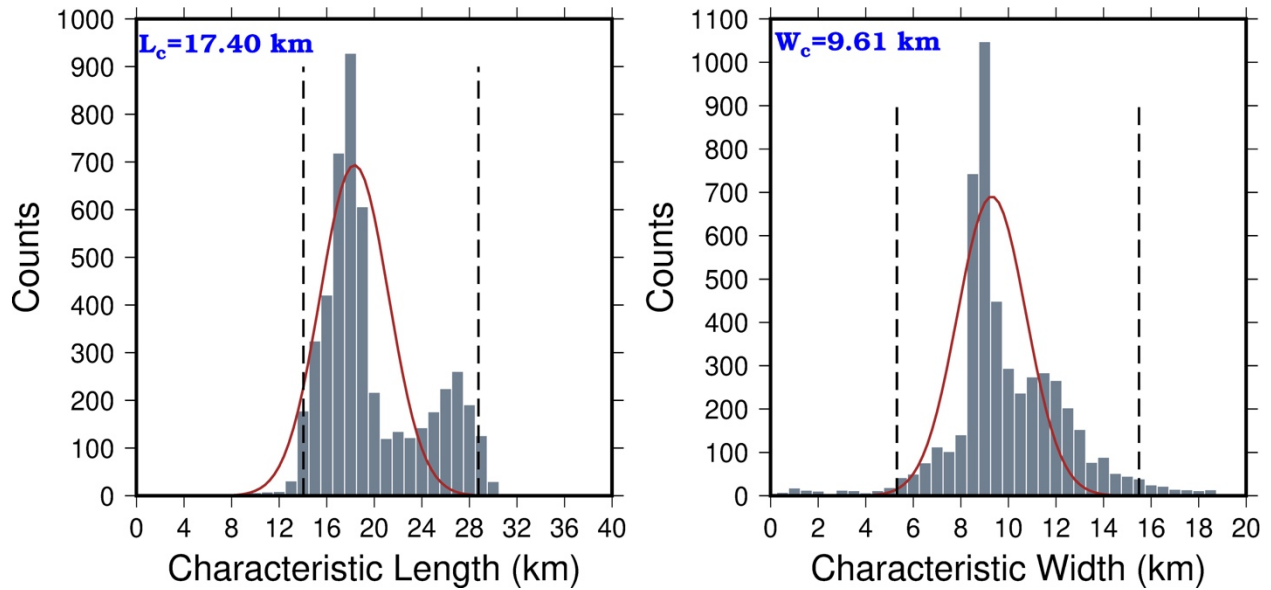


**Figure 3.** Results of deconvolution and bootstrapping. (a) A representative azimuthal distribution of ASTFs (blue traces) plotted at the locations of stations (blue triangles). The epicentre (red star) of the main earthquake is also shown. Note that for clarity, not all ASTFs and stations used in the study are plotted. The average strike (294°) of the fault is projected across

the continent (black dashed-line) to illustrate station distribution relative to the fault plane. ASTFs have a complex form and appear to be longer in the southeast direction (b) shows inversion results of  $L_c$  and  $W_c$  along with bootstrap calculations with 5000 iterations. The brown curve represents the equivalent normal distribution and the black dashed-lines show the 95% confidence interval.

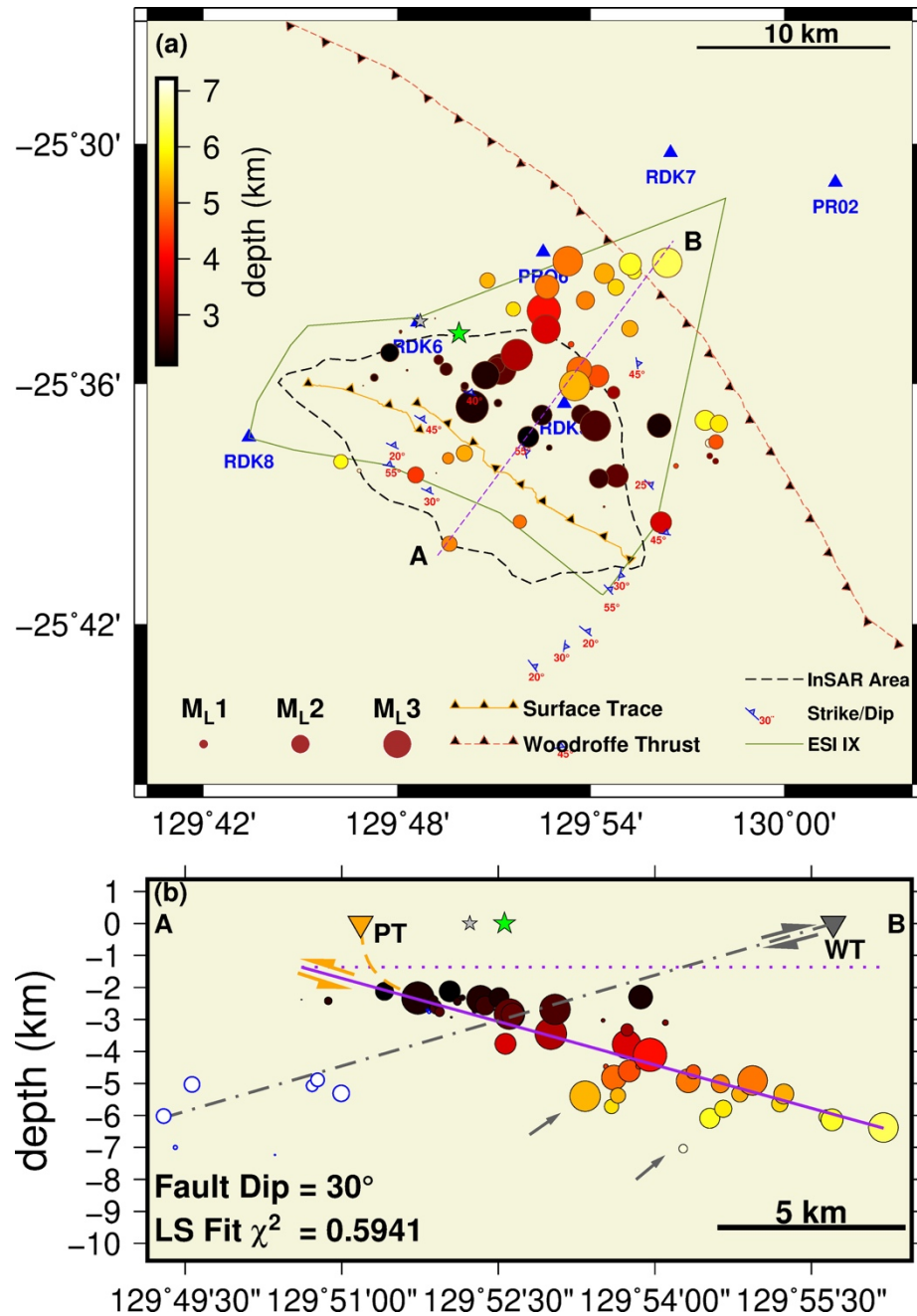


**Figure 4.** The distribution of aftershocks. (a) Map showing the aftershock distribution (solid circles) color-coded by depth along with the surface trace of the Petermann Ranges earthquake (PT) and the Woodroffe Thrust (WT). The epicentres of the main and EGF events are shown with green and grey stars respectively. Six temporary seismic stations are also shown (blue



triangles) while the other three stations are out of the field of view. The depth of aftershocks located to the east of PT increases to the northeast. The environmental seismic intensity (ESI) level IX is represented by the green contour (King et al., 2018). The strike and dip of foliation is from Scrimgeour et al. (1999). The area outlined in Fig. 1 of deformation detected by InSAR image is outlined by dashed-lines. (b) The aftershocks projected on to a cross section along the AB profile shown in (a), which is approximately orthogonal to the average strike of PT. The purple solid line is fitted to color-coded aftershocks using a least squares method, from which the fault dip ( $30^\circ$ ) is estimated (The dotted line is horizontal). The reduced  $\chi^2$  for the least squares fit is also given. The inverted triangles show the surface intersections of PT (orange) and WT (dark grey). The orange dashed-line is arbitrarily drawn to connect PT with the underlying fault plane. The white circles with blue outlines are aftershocks located west of PT. They align with the projected fault plane of WT (dark grey dash-dot line) with a dip of  $20^\circ$  but the dip could vary between  $20^\circ - 30^\circ$  (Stewart, 1995; Neumann, 2013). The grey small arrows point to possible Riedel shears in the foot wall delineated by aftershocks.